Multi-Electrode Extended Gate Field Effect Transistors based on Laser Induced Graphene for Detection of Vitamin C and SARS-CoV-2

Heshmat Asgharian[1,2], Vinay Kammarchedu[1,2,3], Pouya Soltan Khamsi[1,2], Caroline Brustoloni[1,2], and Aida Ebrahimi[1,2,3,4,*]

[1]*Department of Electrical Engineering, The Pennsylvania State University, University Park, PA, 16802, United States*

[2]*Materials Research Institute, The Pennsylvania State University, University Park, PA, 16802, United States*

[3]*Center for Atomically Thin Multifunctional Coatings, The Pennsylvania State University, University Park, PA, 16802, United States*

[4]*Department of Biomedical Engineering, The Pennsylvania State University, University Park, PA, 16802, United States*

*Corresponding author: sue66@psu.edu

Keywords: Laser induced graphene, Ascorbic acid, SARS-CoV-2 virus, Extended gate field effect transistor, Wireless

Abstract

Despite the clinical data showing the importance of ascorbic acid (AA) in managing viral respiratory infections, biosensors for the simultaneous detection of AA or vitamin C and viral infections are lacking. To address this need, we develop a portable and wireless device for detecting AA and SARS-CoV-2 virus, integrating commercial transistors with laser induced graphene (LIG) as the extended gate. We study the effect of laser printing passes and show that with two laser printing passes (2-pass LIG), the sensor sensitivity and limit of detection (LOD) significantly improve by a factor of 1.6 and 12.8, respectively, compared to 1-pass LIG for detecting AA. Using complementary characterization methods, we attribute the improved response to a balanced interplay of crystallinity, defect density, surface area, surface roughness, pore density and diameter, and mechanical integrity/stability. These factors enhance analyte transport, reduce noise/variability, and ensure consistent sensor performance, making 2-pass LIG the most effective material for the LIG-EGFET biosensor. Our sensors exhibit promising performance for detecting AA with selective response in the presence of common salivary interfering molecules, with sensitivity and LOD of 73.67 $\frac{mV}{dec}$ and 54.04 nM in 1× PBS and 81.05 $\frac{mV}{dec}$ and 78.34 nM in artificial saliva, respectively. We also show that functionalization of the 2-pass LIG gate with S-protein antibody enables the detection of SARS-CoV-2 with an ultralow LOD of 52 $\frac{zg}{ml}$ for SARS-CoV-2

S protein antigens – an improvement of more than 10-fold compared to 1-pass LIG – and 4 $\frac{particles}{ml}$ for virion mimics with selective response against influenza virus (H5N1) and multiple human coronavirus strains. The developed portable, multiplexed device, with low drift/hysteresis and wireless capabilities, holds great potential for improving at-home monitoring and clinical decision-making accuracy. Using a dual laser scanning approach, it can detect both AA and SARS-CoV-2 spike protein mimics even in the presence of each other.

Introduction:

Ascorbic acid (AA) – or vitamin C – is one of the most essential micronutrients that the body cannot synthesize and should be taken orally (food, fruits, or supplements).[1] AA can be found in different body fluids, such as plasma, sweet, interstitial fluid, and saliva. Among them, saliva is the most accessible resource for collecting biological compounds with minimal effort and no specialized training. The normal concentration of AA in saliva is around 14 μM (2.5 $\frac{\mu g}{ml}$).[2] It is shown that several diseases, including tuberculosis, parodontopathy, periodontitis (gum disease), cancer, and leprosy can decrease AA concentration in saliva.[3] Importantly, it is shown that the antiviral properties of vitamin C play an important role in the treatment of different viral infections, especially SARS-CoV-2.[4,5] Hence, measuring AA concentration in addition to biomarkers of viral infections is vital for improving the patient care and disease management. The clinical methods to measure the salivary AA level use dichlorophenolinodophenol or dinitophenylhydrazin, relying on antioxidant properties of AA for colorimetric measurements, showing inconsistency in assessing salivary ascorbic acid levels.[3,6] For viral infections, the clinical methods include enzyme-linked immunosorbent assay (ELISA) and quantitative reverse transcription-polymerase chain reaction (qRT-PCR). While critical for clinical needs, the gold standard methods impose some challenges for point-of-care testing, including complexity, time-intensive steps (4-6 h), needing skilled operators (for example, for ribonucleic acid (RNA) extraction), and requiring expensive equipment.[7,8] In addition, these methods are not amenable to scalability and simple use by non-experts. As a result, portable and simple-to-use devices are highly needed for multiplexed detection of low concentrations of AA and viral infections to improve patient outcomes.

Among various devices, extended-gate field-effect transistor (EGFET) is increasingly attractive for developing highly sensitive and stable biosensors. EGFETs address the stability issues and functionalization limitations of conventional field-effect transistors (where the transistor channel material is exposed to the liquid under test)[9,10] by decoupling the transducer part from the sensing part that can be either an external electrode or a metal layer extended from the gate and connect to the transistor gate in the interconnection process known as back-end-of-line (BEOL).[11] The sensing part (extended gate) is separately immersed in the solution consisting of targeted ions or molecules for detection by the sensor. As a result, the channel region of the transducing element is completely separated from the ionic solution and, hence, experiences less drift, hysteresis, and light and temperature sensitivity due to the transistor encapsulation by packaging.[12–14] Moreover, the sensing part is disposable, and the transistor part can be reused, offering flexibility to engineer various sensing electrodes and materials, reducing the device's fabrication complexity and cost.[15]

Different materials such as amorphous indium–gallium zinc oxide (a-IGZO)[16], copper oxide nanowire[17], gallium nitride (GaN) nanowire[18], and carbon dots[19] have been employed as the

extended gate material to enhance the sensitivity and performance of EGFET devices. Among them, carbon-based materials offer distinct advantages owing to their chemical inertness, low cost and environmentally-friendliness, and general biocompatibility.[20] In particular, graphene's electrical properties –made of a planar sp^2-hybridized hexagonal lattice of carbon atoms –can be altered when interacting with charged biomolecules.[21,22] Besides, in several cases, the π–π stacking between the graphene surface and bioreceptors leads to enhanced interaction.[23] Additionally, the oxygen-containing functional groups on the surface of graphene-related materials can be leveraged to enhance the charge transfer in specific reactions.[24] Common routes to obtain/synthesize graphene consist of micromechanical[25] or liquid phase exfoliation[26] as top-down methods and chemical vapor deposition (CVD)[27] or epitaxial growth[28] as example bottom-up techniques. Although high-quality graphene can be synthesized using these methods, they either are incompatible with scalable device miniaturization/fabrication methods or require high-temperature processes, which limits the type of substrates that can be used (increasingly crucial in wearable and flexible devices).[29] In this regard, laser induced graphene (LIG; a 3D porous graphene-based material that can be produced from polymers using CO_2 lasers found in machine shops) has seen exponential interest in the biosensor community,[30] especially to build electrochemical sensors[31–33], FET sensors[34], and stretchable sensors for physical biomarkers and treatment.[35]

In this work, we developed a portable and wireless EGFET-based biosensor for detecting AA and SARS-CoV-2 by integrating commercial transistors with 2-pass LIG as the extended gate. Specifically, we show that the sensor sensitivity and LOD are significantly improved (from 46.43 $\frac{mV}{dec}$ to 73.67 $\frac{mV}{dec}$ and 694 nM to 54.04 nM, respectively) in sensors made using two laser printing passes (2-pass LIG) for selective detection of AA detection in the range of 100 nM to 10 μM. By employing different characterization techniques, we attribute the enhanced response of 2-pass LIG to improved analyte transport, higher crystallinity, less surface roughness (reduced variability), and a balance of defect density, electrical conductivity, and mechanical stability. In addition, by functionalization of the 2-pass LIG gate with S-protein antibody, a wide range of SARS-CoV-2 S protein antigens (Ag(S); 10^{-6} $\frac{pg}{ml}$ to 10^{2} $\frac{pg}{ml}$) and virion mimics (S-mimics; 10 $\frac{particles}{ml}$ to 10^{7} $\frac{particles}{ml}$) can be selectively detected with LOD of 52 $\frac{zg}{ml}$ for Ag(S) and 4 $\frac{particles}{ml}$ for S-mimics. The developed devices also enable multiplexed detection of AA and SARS-CoV-2 in mixtures. We integrated the sensors with a wireless analyzer using off-the-shelf electronic components to develop portable chips with multiple extended gates to simultaneously increase the number of tests. With proper modification, the developed sensing chip can be used to detect other biomarkers and is anticipated to enhance medical care efficiency, especially for at-home monitoring, and improve the accuracy of clinical decision-making processes.

Results and Discussion:

1. Optimization of the LIG-based extended gate:

The configuration of the LIG-EGFET developed in this study is shown in Figure 1, where the transistor gate is connected externally to a LIG electrode (the details of the LIG fabrication process are provided in the Methods: LIG preparation as the extended gate (EG)). We first investigate the effect of the LIG-EG laser printing pass number, which has not been studied in previous LIG-based EGFETs.[36,37] In the following, we show that the sensor performance can be significantly improved by increasing the laser pass number (#). To understand the origin of this enhancement, we perform several characterization methods, including scanning electron microscopy (SEM),

Raman Spectroscopy, and X-ray Diffraction (XRD), in addition to electrical/electrochemical methods to characterize sheet resistance, electrochemical active surface area (ECSA), double-layer capacitance (C_d), and roughness factor (ρ). Moreover, to understand the effect of laser scan number on the pore size and volume, we utilized Brunauer-Emmett-Teller (BET) and Barrett-Joyner-Halenda (BJH) methods.

Figure 2(a) shows the XRD pattern for different laser scan# from 1 to 3, indicating intense peak centered at $2\theta \cong 25.9^{\circ}$ representing (002) plane of graphene. Figure S1 displays the full range of XRD patterns, including peaks at $2\theta \cong 25.9°$ and 44.5°, corresponding to the (002) and (101) graphene planes. Silicon standard peaks have also been incorporated to ensure accurate peak identification and calibration. After the second scan, the (002) peak increased compared to the first and third scans, suggesting a more ordered graphene structure desirable for electronic applications. Figure 2(b) shows the interlayer spacing between (002) graphitic crystal planes in LIG, which decreases with scan number and gets closer to the ideal graphite value (3.3553 Å), resulting in the higher crystallinity and graphitization of LIG.[38] Furthermore, based on the Raman spectra of different scan numbers (shown in Supplementary Information (SI), Figure S2(a)), three primary peaks are observed at ~1345 cm^{-1}, ~1580 cm^{-1}, and ~2690 cm^{-1}, corresponding to the D-band, G-band, and 2D-band, respectively.[39] The D-band is associated with the disorder in the hexagonal carbon lattice and represents the A_{1g} breathing mode at the K-point. The G-band results from the stretching vibrations of sp^2-hybridized carbon atoms within the hexagonal structures, corresponding to the E_{2g} phonon mode at the τ-point.[40,41] The 2D-band is linked to second-order zone-boundary phonons. Additional peaks are also noted at ~2460, ~2930, and ~3230 cm^{-1}, which are attributed to the combinations of T+D and D+G, respectively.[42] Figure 2(c) plots $\frac{I_D}{I_G}$ and estimated crystallite size, L_a ($L_a = 2.4 \times 10^{-10}\lambda^4(\frac{I_D}{I_G})^{-1}$), showing the decrease of defect density and increase of the crystallite size by increasing the scan pass#. Figure 2(d) plots the full width at half maximum (FWHM) of G and 2D peaks, indicating that 2-pass LIG has the lowest FWHM, resulting in a lower disorder in the lattice structure. The FWHM of the 2D band in LIG is a key indicator of graphene's structural quality, particularly regarding disorder and defect density.[43] In 2-pass LIG, the narrower FWHM of the 2D band can be attributed to optimal structural reordering. The laser energy during this scan facilitates defect reduction through annealing effects, improving graphene order without introducing significant new defects. In contrast, 1-pass LIG shows a broader FWHM due to higher initial defect density. While in 3-pass LIG, the third scan reduces some point defects, introducing new ones like strain and stacking disorder, leading to a slight broadening of the 2D band. Thus, the structural integrity with 2-pass LIG balances the defect reduction without over-processing the material. It should be noted that according to the data in Figure 2(d), the FWHM of the G band is slightly lower in 3-pass LIG vs. 2-pass LIG. The FWHM of the G band indicates the number of point defects and the degree of graphitization.[44] Although multiple laser irradiations may have led to the recrystallization of carbon atoms (improving graphitization), we should also consider the FWHM of the 2D band, which represents other types of defects, the layer count of graphene, strain, and electronic band structure. The narrower 2D band FWHM suggests improved quality, decreased level of disorder, and reduced stacks.[43]

Next, we studied the effect of laser scan number on electrical conductivity, surface area/roughness, and porosity of LIG and their correlation to the sensing performance. To understand the impact of laser scan number on electrical conductivity (important in electroanalytical devices), we measured the sheet resistance in Figure 2(e), showing a decreasing

trend by increasing laser pass#. ECSA is also an important metric in electroanalytical sensors, with higher ECSA usually leading to higher sensitivity. Figure 3(a) plots ECSA for different LIG materials (1-, 2-, and 3-pass LIG), showing that 2-pass LIG has the lowest ECSA. Interestingly, 2-pass LIG also has the lowest double-layer capacitance (C_d) and roughness factor (ρ), as plotted in Figure 3(b) and (c). The lower roughness indicates reduced noise and improved sensor stability. It has been previously shown that capacitance depends on pore size distribution and surface chemistry, not just the surface area. Wider micropores and well-regulated surface properties, such as fewer defects and optimized pore distribution, improve performance even in samples with lower surface area. Similarly, 2-pass LIG (with a lower C_d than the 1- and 3-pass samples) has fewer defects and more controlled surface properties.[45] As a result, while lower ECSA indicates reduced electrochemically active sites (consistent with the higher sensitivity of 3-pass LIG compared to 2-pass LIG, see Figure S3 and Table S1), the reduced capacitance in 2-pass LIG minimizes noise compared to 3-pass LIG, leading to a more stable and reliable signal (lower LOD, Figure S3, and Table S1).

While SEM images in Figure S4 show morphological differences across different scan number, for qualitative comparison, we performed BET surface area and BJH pore size and volume analyses (Figure 3 and Table 1). Despite 2-pass LIG showing the lowest ECSA, its BET surface area (Figure 3(d)) is larger than 1-pass LIG (5.26 $\frac{m^2}{g}$ vs. 4.75 $\frac{m^2}{g}$), which compensates for the lower ECSA by offering more overall surface area for biomolecule interactions. The isothermal plot (Figure 3(e)) – which reflects gas adsorption behavior on the material's surface – reveals a more stable and balanced gas adsorption profile. Moreover, the pore volume distribution in 2-pass LIG (Figure 3(f)) is more controlled than in 1-pass LIG, particularly at larger pore diameters (10-50 nm), where the lower pore volume minimizes analyte trapping and improves transport efficiency. The $\frac{dV}{dw}$ pore volume plot (Figure 3(g)) further shows that 2-pass LIG has a tighter distribution of pore sizes, while 3-pass LIG shows broader pore size distribution. This broader distribution can lead to uneven surface characteristics, making it harder to achieve consistent sensor behavior.[46] Collectively, these factors – larger BET surface area, controlled pore volume distribution, and stable adsorption properties – explain why 2-pass LIG is the optimal material in our study despite its lower ECSA.

In conclusion, the combination of lower defects, lower surface roughness (more stability), balanced porosity and electrical conductivity, and controlled pore volume distribution makes 2-pass LIG the optimal choice for the developed LIG-EGFET biosensor. Additionally, the reduced fragility of 2-pass LIG compared to higher laser processed samples further supports its reliability for sensor applications. We believe these findings highlight the complex interplay between LIG structure and sensor performance, where an increase in the surface area or conductivity does not always translate directly into better sensing capabilities. Therefore, we will focus on 2-pass LIG in the following analytical sections for more detailed analysis.

2. Sensor characterization for detection of ascorbic acid:

Next, we evaluate the performance of 2-pass LIG-EGFETs for detecting AA levels. The experiment involves measuring the transfer characteristics $I_{DS} - V_{REF}$ (where V_{REF} is gate voltage sweeping from 0 to 2.5 V) across AA concentrations from 100 nM to 10 μM. $I_{DS} - V_{REF}$ characteristics, such as devices, are shown in Figure S5. The measurements are performed at a low drain voltage (V_{DS} =100 mV) to maintain the MOSFET within the linear operation region. The

performance of the EGFET sensor is evaluated in the strong inversion regime where V_{REF} as the gate voltage is applied to the on-chip silver paste pseudo-reference (Ag-ρRE) electrode and sweeps between 0 to 2.5 V exceeds $V_{T(FET)}$ (the threshold voltage of the commercial MOSFET: $V_{T\,(FET)}$= 1.25 V as measured in Figure S6). Using the $I_{DS} - V_{REF}$ data, we then calculate sensitivity defined as: $S_v = \frac{dV_{REF}}{d\,log_{10}(Conc)} | I_{DS} = const.$ Figure 4(a) plots S_v in different media, showing the sensitivity in a-saliva to be S_v= 81.05 $\frac{mV}{dec}$ compared to 73.67 $\frac{mV}{dec}$ in 1×PBS, which confirms that the sensitivity does not change significantly when changing the medium. Furthermore, the sensor is specific to AA in the presence of interfering molecules (consisting of 300 pM dopamine (DA), 200 µM uric acid (UA), and 300 µM tyrosine (Tyr)) by comparing $\delta(V_{REF} - V_T)$ (which is the baseline-subtracted value of the gate voltage at I_{DS}= 95 µA) in Figure 4(b), showing almost the same performance without interfering molecules and, hence, confirms the selectivity of the devices to AA. It should be noted that the physiological concentration of DA, UA, and Tyr in saliva is < 0.5 nM[47], 180 µM[48], and 400 µM[48,] respectively. Figure S7(a) and (b) show that the sensitivity of the sensors improves in all media by increasing the laser scan# from 1-pass ($S_{v,1xPBS} = 46.43$ $\frac{mV}{dec}$, $S_{v,a-saliva} = 45.48$ $\frac{mV}{dec}$,and $S_{v,mixed\ a-saliva} = 29.3$ $\frac{mV}{dec}$) to 2-pass ($S_{v,1xPBS} = 73.67$ $\frac{mV}{dec}$, $S_{v,a-saliva} = 81.05$ $\frac{mV}{dec}$, and $S_{v,mixed\ a-saliva} = 90.68$ $\frac{mV}{dec}$). In addition, the LOD lso significantly improves from 1-pass LIG ($LOD_{1xPBS} = 694$ nM, $LOD_{a-saliva} = 362.5$ nM, and $LOD_{mixed\ a-saliva} =$ 748 nM) to 2-pass LIG (LOD_{1xPBS} =54.04 nM, $LOD_{a-saliva}$ =78.34 nM, and $LOD_{mixed\ a-saliva} =$ 112.24 nM), see Figure S8(a) and (b).

In addition to the static tests discussed above, Figure 4(c) plots real time measurement with different concentrations of AA in 1×PBS collected at $V_{REF} = 1.5$ V and $V_{DS} = 0.1$ V. Moreover, our sensors show negligible hysteresis of 1.5, 0.74, and 1.85 mV (lower than 4 mV) in 1×PBS, a-saliva, and mixed a-saliva, respectively, across repeated measurements with the same AA concentration (5 µM), as shown in Figure S9(a-c). Such low hysteresis is caused by using a commercial MOSFET, which is critical for stable readout. We also evaluate our sensor's reusability and shelf life by testing over 12 days, Figure 4(d) and (e). We tested the same devices every two days at constant AA concentration (5 µM) to determine reusability. To evaluate the device shelf life, we fabricated the devices on the same day, and every two days, new devices were tested at constant AA concentration (5 µM). The sensors show a drift value of 0.33 $\frac{mV}{h}$ and 0.12 $\frac{mV}{h}$ for reusability and shelf life, respectively.

Of note, there is an initial signal drop from day 0 to day 4 in Figure 4(d). This drop may be related to an initial material stabilization period. This material "annealing" may occur, for example, due to surface functionalization of LIG with oxygen groups due to prolonged exposure to air, acting as a doping mechanism.[49] During the first few days of repeated use, the device undergoes a natural conditioning process where minor adjustments in the surface chemistry and interface states of the LIG material occur. These adjustments may also result from repeated testing, slight reorganization of the surface structure, or relaxation of any initial stresses introduced during fabrication or early testing cycles.[50] It is important to note that this is a transient effect. By day 4, the device has reached a stable operating state, as evidenced by the minimal drift observed thereafter. It should be, however, noted that the developed devices are meant for single-use operation; hence, the more relevant/important signal drift is related to shelf life (Figure 4(e)), which shows a very stable behavior. In addition, with SARS-CoV-2 sensing, two main factors can affect the shelf life and reusability: the LIG itself and the antibody (known to be sensitive to

environmental parameters such as temperature[51]). Hence, to focus on the stability of LIG itself over time in the context of EGFET operation, the current work focuses on AA for reusability and stability testing.

In order to show the significant sensing improvement by using LIG in EGFET compared to conventional voltammetry methods, we also performed cyclic voltammetry (CV) and differential pulse voltammetry (DPV), clearly showing their inability to detect nM levels of AA while also suffering from significant noise (Figure S10). Figure S10(a-b) show that CV and DPV have a poor sensitivity toward AA (1 nM-400 μM) with LOD of 207 μM and 0.1 μM, respectively. Finally, to further demonstrate the advantage of LIG compared to other commonly used and low-cost carbon/graphene electrodes, we measured the ECSA of LIG, graphene ink, and glassy carbon electrode (GCE). To determine ECSA, CV characteristics with different scan rates are performed in 5 mM of ferrocyanide-ferricyanide mixture (Figure S11), showing that the anodic and cathodic currents are linear vs. the square root of the scan rate.[32] As summarized in Table S2, LIG offers the highest ECSA (normalized to the geometrical surface area) and, hence, provides more active sites for molecular interactions.

Finally, it should be noted that in our work, the silver paste applied to the LIG electrode serves as an on-chip ρRE. On-chip reference electrodes are important when developing portable and compact diagnostic devices.[52,53] To confirm the suitability of Ag-ρRE in our work, we compared the performance of Ag-ρRE to a standard glass Ag/AgCl electrode for EGFET tests. Figure S12(a) shows that Ag-ρRE is highly stable and performs well for on-chip testing. In addition, to ensure the stability of ρRE, we monitor the gate leakage current, which is < 0.4 nA (Figure S12(b)), confirming good device stability.

3. Understanding the mechanism of selectivity to ascorbic acid:

To understand the mechanism for selectivity of LIG to AA, we performed X-ray photoelectron spectroscopy (XPS). Figure S13(a) shows a detailed fitting of the C1s spectrum of pristine LIG and after adding AA (500 μM) to LIG before and after washing with 1×PBS. The additional peaks observed at 293 eV and 295 eV in the XPS spectrum of Figure S13(a: i and ii) following the treatment of laser-induced graphene with 1×PBS are likely satellite peaks associated with phosphorus 2p electrons from phosphate groups.[54] Before discussing the XPS data, the data in Figure S5 shows that the drain current decreases (threshold voltage increases) by increasing AA concentrations. This behavior is associated with the electron transfer of AA to LIG-EG, changing the electrode's surface potential and, as a result, changing the threshold voltage. At physiological pH = 7, AA mostly appears as an ascorbate anion due to having a pK_a of 4.24. Ascorbate anion first loses one proton and one electron, while an additional single electron transfer characterizes the subsequent phase.[55,56] Also, AA contains multiple hydroxyl groups capable of forming strong hydrogen bonds[55–58], which enhances its interaction with the LIG surface. This strong hydrogen bonding facilitates efficient electron transfer (ET), as AA readily donates electrons through its enediol group[55,56], significantly altering the surface potential of the LIG extended gate. In contrast, DA, UA, and Tyr – among potential interfering molecules found in saliva – have fewer hydrogen bond-forming groups and different oxidation mechanisms, exhibiting weaker interactions and less efficient electron transfer. Furthermore, the oxygen-containing functional groups on graphene-based materials facilitate selective electrocatalytic oxidation of the enediol group in AA.[24] The oxygen-containing functional groups extract two protons from the enediol groups, which trigger AA's electron loss/donation. This interfacial interaction results in the depletion of oxygen functional groups on LIG, consistent with the atomic percentage changes observed in the XPS data

(Figure 5). The XPS results reveal that after the introduction of ascorbic acid (500 μM in 1×PBS; other concentrations show similar behavior and are shown in Figure S13(b)), a reduction in oxygen functional groups (O-C=O, C=O, and C-O) appears. This interaction increases the negative charge density at the surface of the LIG-EG, resulting in a right shift of $I_{DS} - V_{REF}$ in the utilized n-channel MOSFET (*i.e.* increase of $V_{T(EGFET)}$).[59] Notably, after washing with 1×PBS, these oxygen functional groups exhibit a resurgence to their pre-interaction levels, indicative of the physisorption interaction between AA on LIG, which is characterized by non-covalent physisorption-based interactions consistent with the formation of hydrogen bonds rather than covalent bonds. The transient reduction of oxygen functionalities and their subsequent recovery post-washing underscores the potential for the LIG-based EGFET device's reusability.

4. Sensor characterization for detection of SARS-CoV-2 virus:

Next, we demonstrate the ability of the LIG-EGFET devices to detect viral infections (with SARS-CoV-2 as a model pathogen) by functionalizing EG-LIG with antibodies. The different functionalization steps are explained in the Methods: LIG functionalization for SARS-CoV-2 antigen detection). As can be seen in Figure 6(a), the threshold voltage of the device decreases after PBA functionalization, which is due to the p-doping effect of the pyrene group.[60]After adding antibody and BSA, the drain current shifts to the right, resulting in an increase of the threshold voltage due to n-doping of antibody.[61,62] The observed shift towards higher threshold voltages after S-protein antigen hybridization indicates that the complementary antigens can effectively interact with LIG, causing an n-doping effect based on the graphene-protein interaction. Figures 6(b) and (c) show the signals collected using 1-pass and 2-pass LIG-based EGFET devices for a wide range of antigen concentrations from 10^{-6} $\frac{pg}{ml}$ to 10^{2} $\frac{pg}{ml}$. It should be noted that similar to AA, not only are LOD and sensitivity significantly enhanced by increasing the laser print pass # from 1 to 2 (improvement of more than 10-fold and 2-fold, respectively), but noise is also significantly reduced.

In addition to antigen fragments, we analyzed the sensor response to virion mimics (antigen-coated polymer beads with similar size and surface charge as SARS-CoV-2). Compared to antigen fragments, mimics better represent the physical and electrical characteristics of the actual virus particles. Figure 6(d) and (e) show the sensitivity and selectivity tests using SARS CoV-2 S mimics in 1×PBS with 2-pass LIG. Remarkably, Figure 6(d) indicates that the device can detect SARS-CoV-2 S virion mimics at an exceptionally low concentration, achieving a detection limit of ~ 4 $\frac{particles}{ml}$. This sensitivity is particularly notable as it suggests the sensor's potential for early-stage virus detection. Specificity tests are presented in Figure 6(e), where the sensor's response to a variety of non-target viruses (mimics) is assessed under identical conditions. The results highlight the sensor's selectivity for SARS-CoV-2 against influenza H5N1 and various human coronavirus strains (HCoV-229E, HCoV-NL63, HCoV-OC43). Also, the isoelectric point (*PI*) value of SARS CoV-2 S virus and most of the viruses is lower than 7, confirming their negative charge at pH of 7.[63,64]

5. Detection of ascorbic acid and SARS-CoV-2 in mixed solutions

To evaluate the performance of our sensors in detecting AA and SARS-CoV-2 in the presence of the other one, we conducted a series of tests in solutions containing both analytes. Figure 7(a) illustrates the response of the sensor to various concentrations of AA (100 nM- 10 μM) in 1×PBS

in the presence of $10^5 \frac{particles}{ml}$ SARS-CoV-2 mimics in comparison to the data in the absence of the mimics. The results, collected using the sensors without antibody, indicate that the AA signal does not change much in the presence of the virus. To study the effect of AA in response to SARS-CoV-2 mimics, we tested antibody-functionalized sensors with mimics mixed with two concentrations of AA (500 nM and 1 μM) and compared them to the data in the absence of AA, Figure 7(b). The data demonstrates that the device maintains high sensitivity and reliability in detecting virus mimics. The sensor's ability to detect each analyte in mixtures underscores its potential for multiplexed detection of AA and SARS-CoV-2.

6. Developing a wireless and portable chip with a multi-gate configuration:

To demonstrate the potential of the LIG-EGFET sensors for point-of-care remote testing, we developed a portable, wireless sensing system integrated with the LIG-EGFET with multi-gate electrodes (as depicted in Figure 8(a)). The multi-EG device consists of six sensors connected to the commercial MOSFET as a transducer (more information regarding printed circuit board (PCB) board design is provided in Methods: Design of the PCB for portable and wireless multi-gate reading and Figure S14). Figure S14(a: i and ii) show pin connections and PCB board design in the top and back view of the wireless device. Fig. S14(b: i and ii) show the optical images of a device in top and back view by specifying PCB board components. Also, Figure S14(b: iii) shows six LIG-based EG connected via pin ZIF connector to the PCB board. Figure S14(c) shows the portability of the proposed device. As shown in Video S1, we first measure 1×PBS to calibrate the wireless devices. Then AA (100 nM as an example in Video S1) is added to show the proof of concept for applying the developed system as a portable and wireless diagnostic device. The calibration curve measured using the wireless system with the developed readout circuit is consistent with that of the source-measurement unit (SMU), as illustrated in Figure 8(b).

Before concluding, the original contribution of the present work can be summarized as:

(1) Establishing process (laser scan number)-property-performance relationship: we boosted the limitation of low detection of AA and SARS CoV-2 S virus by studying the effect of laser pass number in creating LIG. In particular, using various complementary characterization techniques, we studied the effect of laser scan number on LIG porosity, surface area, surface roughness, defect density, crystallinity, and conductivity to identify the key parameters that lead to an optimal response with LIG-EGFET devices.

(2) Sensing application by demonstrating two case studies (AA as an immobilization-free and SARS-CoV-2 as an immobilization-based model sensing scheme): we showed that both AA and SARS-CoV-2 virions can be detected using the developed low-cost, portable and user-friendly method. Simultaneous detection of AA and virus has important implications for patient care because there are several clinical data on the antiviral properties of vitamin C being beneficial for the treatment of different viral infections, especially SARS-CoV-2.[4,5,65] Detection of low concentrations of AA is critical due to incapability of the body to synthesize it and limitation of existing methods. We compared the performance of the developed EGFET sensor with other potentiometric sensors for ascorbic acid and SARS-CoV-2 antigens in Table S3 and Table S4, respectively. Our sensors exhibit good sensitivity, selectivity, and a lower LOD for AA, underscoring its exceptional performance in various environments. Moreover, our sensors demonstrate a hysteresis-free response with minimal drift voltage, ensuring precise and stable measurements over time. In addition, as summarized in Table S4, our sensors demonstrate an outstanding response to SARS-CoV-2 virus Ag(S) and S-mimics, boasting the lowest LOD, to the

best of our knowledge, amongst other reported methods such as diagnostic test kit, electrochemical, optical, and FET-based methods (52 $\frac{zg}{ml}$ for Ag(S) and 4 $\frac{particles}{ml}$ for S-mimics). The impressive performance of the developed device, combined with multi-gate electrodes, allows for reliable detection of multiple analytes, further highlighting its versatility and potential use for clinical applications. Additionally, its portable and wireless design offers convenience and flexibility, making it a promising candidate for widespread adoption in point-of-care diagnostics.

Conclusions:

In this work, we developed LIG-based EGFETs for simultaneous detection of ultralow concentrations of AA and SARS-CoV-2 by optimizing the laser pass number in creating LIG extended gate electrodes. Using 2-pass LIG as the extended gate, the sensors exhibit significantly better sensitivity and LOD compared to 1-pass LIG in various media. Notably, the sensors demonstrate a selective response to AA, with a sensitivity and LOD of 90.68 $\frac{mV}{dec}$ and 112.24 nM, respectively, in a-saliva containing AA and common salivary interfering molecules. By functionalizing the 2-pass LIG gate with S-protein antibody, the developed EGFET-based biosensor can successfully detect a wide range of SARS-CoV-2 S protein antigens and virion mimics. In particular, the sensors achieve an ultralow LOD of 52 $\frac{zg}{ml}$ for antigens, which is an improvement of more than 10-fold in LOD with a 2-fold increase of sensitivity compared to 1-pass LIG. We correlate the improved response of 2-pass LIG to enhanced analyte transport and crystallinity, reduced noise, and a balance of defect density, conductivity, and mechanical integrity. The sensors also exhibit selective performance toward SARS-CoV-2 when tested with other viruses, such as influenza H5N1 and various human coronavirus strains (HCoV-229E, HCoV-NL63, and HCoV-OC43). To illustrate the accessibility for point-of-care testing, the devices are integrated with a wireless analyzer, enabling real-time data transmission and remote monitoring. The developed low-cost, portable devices can potentially improve patient care given the existing clinical data supporting the antiviral properties of vitamin C, especially against SARS-CoV-2. In addition, the present multi-gate EGFET-based biosensor can be further tailored to detect other biomarkers, ultimately enhancing clinical decision-making and improving the efficiency of medical care.

Methods:

Materials and reagents:

L-ascorbic acid (A5960), dopamine hydrochloride (H8502), uric acid (U0881), L-tyrosine (T3754), 1-Pyrenebutyric acid (PBA, 257354), N-Hydroxysulfosuccinimide sodium salt (Sulfo-NHS, 56485), N-Dimethylformamide (DMF, D4551), bovine serum albumin (BSA, A437), ammonium chloride (31107), calcium chloride (C1016), potassium thiocyanate (KSCN, 207799), sodium chloride (S3014), potassium chloride (P9541), MES hydrate (M2933), citric acid (251275), TWEEN® 20 (P1379), EDAC (1-ethyl-3-(3-dimethyl aminopropyl) carbodiimide) from Millipore Sigma (E6383), hydrochloric acid, hydrochloric acid (CAS#: 7647-01-0), sodium hydroxide solution (CAS#: 1310-73-2), glycine (CAS#: 56-40-6), sodium azide (CAS#: 26628-22-8), graphene ink (900960), toluene (179418), potassium hexacyanoferrate(II) trihydrate (potassium ferrocyanide, 1.04984) and potassium hexacyanoferrate(III) (potassium ferricyanide, 60299) were all obtained from Sigma-Aldrich. EDC (1-ethyl-3-(3-dimethylaminopropyl) carbodiimide hydrochloride) (22980) was purchased from Thermos Scientific. Isopropyl alcohol (IPA) (67-63-0) and SARS-COV-2 S Protein HIS Tag (CAS: 103871-150) were obtained from

VWR International, LLC. Influenza H5N1 (A/Hubei/1/2010) Neuraminidase / NA (His Tag) (CAS: 40018-V07H), Human coronavirus (HCoV-229E) Spike/S1 Protein (S1 Subunit, His Tag) (CAS: 40601-V0BH), Human coronavirus (HCoV-OC43) Spike S1 Protein (His Tag) (CAS: 40607-V08H1), Human coronavirus (HCoV-NL63) Spike/S1 Protein (S1 Subunit, HIS Tag) (CAS: 40600-V08H), and SARS-CoV-2 (2019 nCoV) Spike S2 Antibody Affinity Purified (CAS: 40590-T62) were obtained from sino biological. Dulbecco's Phosphate Buffered Saline (DPBS) 1x was purchased from Corning. DuPont™ Kapton® polyimide (PI) film with thickness and width of 0.005″ and 12″ respectively, was obtained from American durafilm. A silicon wafer (4″ P <100>. 0.001-0.005 ohm-cm) with wet thermal oxide on both sides was purchased from Nova Electronic Materials. A glassy carbon electrode (MF-2012) was purchased from BASI research products. Ultrapure deionized water (DI) (18.2 MΩ cm) was used in all our experiments.

LIG preparation as the EG:

First, the PI sheet is rinsed with IPA, dried with dry clean air, and mounted on the metal workbench of a commercial laser cutter (VLS2.30, Universal Laser Systems, Inc.) using tapes at the edges. To reach good conductivity and structural integrity, the laser beam is focused, and laser power, speed, and resolution are adjusted to 12.6%, 5.5%, and 1000 pixels per inch (PPI), respectively, in raster mode. Our laser printer has a maximum power and speed of 30 W and 762 $\frac{\text{mm}}{\text{s}}$, respectively (Figure 1(a)). The sensing compartment of the EGFET has two LIG-based electrodes (designed in AutoCAD software) as shown in Figure 1(b): the extended gate and the ρRE, which is made by applying silver conductive epoxy Adhesive (MG Chemicals 8331D, dried for one h in the lab ambient environment). Figure 1(c) shows EG for AA and SARS-CoV-2 virus detection.

FET measurements:

The measurements were performed with two Keithley (6430) to apply gate and drain voltage. To operate in the linear region of commercial MOSFET (CD4007UBE, Texas Instruments, DigyKey), drain voltage was set at 0.1 V, and gate voltage was swept from 0 to 2.5 V with step of 0.05 V. Real time measurement was done by fixing drain and gate voltage at 0.1 and 1.5 V respectively.

Electrochemical measurements:

MultiPalmsens and PalmSens were used as commercial potentiates to perform CV and DPV as the standard voltammetry measurements. CV and DPV tests of AA were done with three electrode designs (working electrode (WE): LIG, counter electrode (CE): LIG, and pseudo reference electrode (pRE). The CV was performed from -0.4 V to 0.7 V with 10 mV step, scan rate of 50 $\frac{mV}{s}$, and three scanning. DPV was done from -0.3 V to 0.7 V with the step of 5 mV, scan rate of 10 $\frac{mV}{s}$, and scanning number of three. CV tests of different WEs (LIG, graphene ink, and glassy carbon electrode (GCE)), CE (platinum), and commercial Ag/AgCl glass reference electrode (MF-2052, Bioanalytical Systems, Inc) were done in potassium ferrocyanide/potassium ferricyanide (5mM) by applying voltage from -0.5 V to 1 V with step of 10 mV, scan number of 3, and different scan rate (10 $\frac{mV}{s}$, 50 $\frac{mV}{s}$, 100 $\frac{mV}{s}$, 150 $\frac{mV}{s}$, 200 $\frac{mV}{s}$, and 500 $\frac{mV}{s}$) to calculate electrochemically active surface area (ECSA).

Reusability and shelf-life measurement:

Our sensor's reusability and shelf life are done by testing the devices over 12 days. We tested the same devices every two days at constant AA concentration (5 μM) to determine reusability. To

evaluate the device shelf life, we fabricated the devices on the same day, and every two days, new devices were tested at constant AA concentration (5 µM). The sensors were stored in the desiccator with nitrogen gas and controlled humidity.

Double layer capacitance and roughness factor calculation:

To calculate the electrode's double-layer capacitance and roughness factor, the geometrical area of the electrode (A_g) was determined using the electrode diameter (d =1.5 mm): $A_g = \frac{\pi d^2}{4}$. The background charging current (i_{BG}) was obtained through CV measurements of the LIG electrode in 1×PBS, with the potential scanned from -0.4 V to +0.7 V at a scan rate of 50 $\frac{mV}{s}$, measured at 0.0 V vs. RE. The double-layer capacitance (C_d), expressed in $\frac{\mu F}{Cm^2}$ was then calculated, where υ represents the CV scan rate: $C_d = \frac{i_{BG}}{\upsilon A_g}$. The roughness factor ($\rho$), representing the ratio of the microscopic area (A_m) to the geometrical area (A_g), was determined using $\rho = \frac{A_m}{A_g}$. This was estimated by comparing the C_d of the LIG electrode with that of the GCE, where $C_d(GCE) = 27.7\ \frac{\mu F}{cm^2}$, considered characteristic of a flat carbon surface.[66]

ECSA calculation:

ECSA is calculated according to the Randles-Sevcik equation[67]: $i_p = (2.69 \times 10^5) n^{3/2} A D_0^{1/2} C_0^* \upsilon^{1/2}$, where i_p is peak current (A), n is the number of transferred electrons per reaction, D_0 *is* the diffusion coefficient of the reactant in the electrolyte (D: $7.63 \times 10^{-6}\ \frac{cm^2}{s}$), C is the concentration of the reactant in the bulk ($5 \times 10^{-6}\ \frac{mol}{cm^3}$), υ is the scan rate ($0.1\ \frac{V}{s}$), and A is the electrochemically active surface area (cm^2).

Sheet resistance measurements:

The LIG is fabricated in a rectangular shape (l = 2cm, and w = 1 cm) and homebuilt four-point probe setup. Keithley 2450 was used for measuring sheet resistance. The sheet resistance is calculated through $R_s = \frac{\pi}{\ln 2}\frac{\Delta V}{I} \times correction\ factor = 4.53236 \times R \times correction\ factor$, where ΔV is the potential difference, and I is the current between the probes. In our case, the correction factor is 0.7115.

Graphene ink preparation:

First, the SiO_2 wafer was cut into 1cm × 1cm pieces. Then, it is cleaned with acetone and IPA through bath sonication for 15 minutes. After cleaning, the sample is placed in 5% toluene solution (1 ml DMF + 19 ml Toluene) overnight. Then, the sample is removed from 5% DMF + toluene solution, washed with Toluene, and dried with air. The sample is placed in spin coated with 5000 rpm for 30~35s and then 60 µl graphene ink is drop cast onto the sample. Finally, it was placed on the hotplate (300˚ C) for 30 minutes.

Design of the PCB for portable and wireless multi-gate reading:

The main component of the PCB is an ESP32 microcontroller, chosen for its integrated analog-to-digital (ADC) and digital-to-analog converters (DAC), along with wireless communication (Bluetooth and Wi-Fi) capabilities. The microcontroller is connected to the PC using CP2104 USB

to serial converter chip via a micro-USB port, which is also used to charge the integrated 350 mAh Li-Po battery using MCP73831T charge controller chip. The battery can power the device for 6 hours, allowing for field measurements and remote applications. AP2112-3.3 is used as the voltage regulator to power the onboard electronics. CD4007UBE MOSFETs are employed as the transistors in the EGFET devices, selected for their compatibility and performance characteristics with graphene-based applications. The DACs of the ESP32 set the gate and source-drain potentials. Contact to 6 LIG-EGs is made via a 12-pin ZIF connector. TLC2264 operational amplifiers are utilized to construct transimpedance amplifiers, which are critical for converting the EGFET current output to a voltage signal measured by the ADCs of ESP32 and wirelessly transmitted using Bluetooth. All off-the-shelf components are purchased from DigiKey Co.

LIG functionalization for SARS-CoV-2 antigen detection:

At first, 10 µL 1-Pyrenebutyric acid (PBA) in dimethylformamide (DMF; (5mM) is drop cast on LIG-EG and incubated for 2 hours in a humidity chamber (97% humidity). After 2 hours, the electrode is rinsed with DMF, IPA, and DIW and dried with nitrogen gas. Next, 10 µl of 0.4 M EDC/0.1 M Sulfo-NHS in 25 mM MES buffer is drop cast on the electrode and incubated for 35 minutes in the humidity chamber (97% humidity). To obtain 0.4 M EDC and 0.1 Sulfo-NHS in MES, 7.668 mg EDC and 2.173 mg Sulfo-NHS are dissolved in 100 µL MES. Afterward, the electrode is rinsed with MES buffer and dried with nitrogen gas. Then, 10 µL SARS-CoV-2 (2019 nCoV) Spike S2 antibody is drop cast on LIG-EG, followed by incubation for 3 hours at 4^{o}C. Next, the LIG-EG is rinsed with 1×PBS and dried with nitrogen gas, followed by drop casting 10 µL Bovine Serum Albumin (BSA) and incubation for 1.5 hours in ambient conditions. To make BSA, 2.5 mg BSA powder is dissolved in 2.5 mL 1×PBS and 2.5 µL tween, then stored at 4^{o}C for 15-30 minutes to dissolve. After incubation with BSA, LIG-EG is rinsed in 1×PBS and dried with nitrogen gas. Finally, different antigen concentrations are added to the EG electrode, followed by the electrical measurement. It should be noted that when depositing the antigen solution, it is mixed by pipetting (gently over the electrode) for 30 seconds and incubating for 2.30 minutes.

SARS CoV-2 S mimics preparation:

The SARS-CoV-2 virion mimics are created using the process detailed in Ref. [68]. Briefly, 10 µL of the antigens from an aliquoted stock was first dissolved in 720 µL of MES buffer in a glass centrifuge tube to make a 60 µg/mL antigen solution as the target analyte and HCoV-229E antigen protein; then, 270 µL of a 4% aqueous suspension of carboxylate-modified microspheres latex bead with 100nm (Invitrogen, U.S.) was added to the antigen solution. The mixture was incubated at room temperature for 15 minutes. Following the incubation, 10 mg of EDAC (1-ethyl-3-(3-dimethyl aminopropyl) carbodiimide) was added to the mixture and mixed by vertexing. The reaction mixture was further incubated on a rocker orbital shaker for 2 hours at room temperature. Agglomeration of the particles may be observed at this point. This can be addressed by adjusting the pH to 6.5 (hydrochloric acid and sodium hydroxide solution as needed) and sonicating the mixture in a sonicator bath. After the incubation, 7.5 mg of glycine was added to achieve a final concentration of 100 mM to quench the reaction. The mixture was then incubated for an additional 30 minutes at room temperature. The virus mimics were then separated from unreacted proteins by centrifuging the sample at 25,000 × g for 30–60 minutes. The pellet was resuspended in 1 mL of 50 mM PBS by gentle vortexing, and the sample was centrifuged again at 25,000 × g for 30–60 minutes. This washing step was repeated twice more for a total of three washes. After the final wash, the virus mimics were resuspended in 1500 µL of 50 mM PBS, which also contains 1% to help provide a more stable suspension. Finally, 130 µg (2 mM) of sodium azide was added to the

suspension, and the virus mimics were stored at 4°C before use. Sodium azide acts as a preservative, with typical concentrations ranging from 0.02% to 0.2% for this purpose. In this process, we used 50 mM phosphate buffer saline (PBS), pH 7.4, containing 0.9% NaCl. 50 mM MES buffer, pH 6.0, was also prepared by dissolving 0.11 g of MES monohydrate in 500 ml deionized water and adjusting the pH by adding hydrochloric acid and sodium hydroxide solution as needed.

Preparation of artificial saliva:

Artificial saliva was made by mixing 5 mM of sodium chloride (NaCl), 1 mM of calcium chloride ($CaCl_2$), 15 mM of Potassium chloride (KCl), 1 mM of citric acid, 1.1 mM of potassium thiocyanate (KSCN), and 4 mM of ammonium chloride (NH_4Cl) into DI water. The pH level was set to 6.7 to match the typical saliva pH in a healthy person.[69]

Material characterization:

SEM micrographs were taken using an Apreo instrument (Thermo Fisher Scientific). To prepare the LIG for XRD analysis, LIG is patterned into a 1 cm² rectangular structure (15 to 20 samples). Then, the LIG is carefully removed from its substrate using a blade that is not very sharp, which converts it to powder. Powders were front-loaded into a silicon zero background holder, and diffraction data were collected from 5 to 70° 2θ using a Malvern Panalytical Empyrean® instrument fitted with a copper (Kα1=1.540598 Kα2 1.544426 Å) long-fine-focus X-ray tube operated at 45 kV and 40 mA. The incident beam path included iCore® optics fitted with a BBHD® optic with 0.03 radian Soller slits, a 14 mm primary and a 14 mm secondary mask, and a fixed 1/4° divergence slit. The diffracted beam path incorporated dCore® optics with a 1/4° fixed anti-scatter slit and 0.04 radian Soller slits. A PIXcel3D® detector was used in scanning line (1D) mode with an active length of 3.347° 2θ. Data were collected with a nominal step size of 0.026° 2θ. PHD lower and upper levels were set at 4.02 and 11.27 keV, respectively. Phase ID was carried out using Jade® software (version 8.9) from Materials Data Inc. (MDI) and the International Centre for Diffraction Data (ICDD) PDF5® database. The d-values were calculated using a Pseudo-Voigt profile fit in Jade version 8.9 from Materials Data Incorporated (MDI) software. The software converts the 2-theta position from the profiles into d-values using Bragg's Law. The X-ray diffraction patterns were calibrated using silicon as an internal standard to obtain accurate two-theta angles and, therefore, accurate d-spacings. XPS analyses were conducted with a Physical Electronics VersaProbe II system (Chanhassen, MN) utilizing an Al Kα X-ray source at a 45° takeoff angle. Charge neutralization involved using low-energy electrons and Ar ions (both <5 eV). Charge calibration was achieved by referencing the sp2 carbon peak at 284.4 eV, employing a pass energy of 23.5 eV. Additionally, Raman spectroscopy was performed using a Horiba LabRam device (Kyoto, Japan) equipped with a 100x objective and an 1800 g/mm grating. A 532 nm laser was employed at 5% of its 110mW capacity. The Raman and XPS spectra were analyzed using LabSpec 6 and CasaXPS software, respectively. For BET surface area and BJH pore size and volume analyses, the sample(s) were loaded into a 1/2-inch outer diameter tube using a glass funnel with a long stem. Sample tube setup included check seals and filler rods. The sample(s) were first put under a vacuum at 30 degrees C for a 10-minute degas followed by a degas with a heating step of 150 degrees C for over 70 Hrs on a Smart VacPrep (Micromeritics; GA, U.S.A.). Data was collected using a Tristar II Plus surface area/porosity analyzer. (Micromeritics; GA, U.S.A.) An 88-point ISO Therm test was performed using nitrogen as the absorbent. Equilibrium time was set at 10 seconds per point.

Supporting Information:

X-ray Diffraction (XRD) analysis, Raman spectra, Sensitivity and Limit of Detection (LOD) of LIG-EGFET with different laser scan# of laser induced graphene (LIG), scanning electron microscopy (SEM) images, transfer characteristics of EGEFT, Commercial MOSFET characteristic, Sensitivity, Repeatability, drift, cyclic voltammetry (CV) and differential pulse voltammetry (DPV), Anodic and cathodic peaks, On-chip Ag paste, Leakage current, X-ray photoelectron spectroscopy (XPS), Portable and wireless multichannel printed circuit board (PCB) design, Calculated electrochemically active surface area (ECSA), Performance comparison of potentiometric methods for AA detection, Comparison of different methods for rapid detection of SARS-CoV-2 antigens.

Acknowledgment.:

The authors would like to acknowledge partial funding from the NSF:I/UCRC Center for Atomically Thin Multifunctional Coatings (ATOMIC) under the Division of Engineering Education and Centers (Award No. 2113864), the NSF Division of Electrical, Communications and Cyber Systems (ECCS, Award No. 2236997), and the National Institutes of Health (Award No. R21EB031354). The content of this report is solely the responsibility of the authors and does not necessarily represent the official views of the NSF or NIH. Additionally, the authors thank the Materials Characterization Lab (MCL) at the Penn State Materials Research Institute, especially Dr. Nichole M. Wonderling, Dr. Jeff Shallenberger, and Mr. Gino Tambourine for their support with the XRD, XPS, BET, and BJH measurements and analysis. Also, the authors appreciate Mr. Peyman Asadi for his help with the graphics in the schematics shown in Figure 1 and Figure 7(a).

References:

(1) Padayatty, S. J.; Levine, M. Vitamin C: The Known and the Unknown and Goldilocks. *Oral Dis* **2016**, *22* (6), 463–493. https://doi.org/10.1111/odi.12446.

(2) Stuteville, O. H. Presence of Vitamin C in Saliva. *Proceedings of the Society for Experimental Biology and Medicine* **1935**, *32* (9), 1454–1455. https://doi.org/10.3181/00379727-32-8132P.

(3) Evans, L. W.; Omaye, S. T. Use of Saliva Biomarkers to Monitor Efficacy of Vitamin C in Exercise-Induced Oxidative Stress. *Antioxidants* **2017**, *6* (1), 5. https://doi.org/10.3390/antiox6010005.

(4) Colunga Biancatelli, R. M. L.; Berrill, M.; Marik, P. E. The Antiviral Properties of Vitamin C. *Expert Rev Anti Infect Ther* **2020**, *18* (2), 99–101. https://doi.org/10.1080/14787210.2020.1706483.

(5) Shahbaz, U.; Fatima, N.; Basharat, S.; Bibi, A.; Yu, X.; Hussain, M. I.; Nasrullah, M. Role of Vitamin C in Preventing of COVID-19 Infection, Progression and Severity. *AIMS Microbiol* **2022**, *8* (1), 108–124. https://doi.org/10.3934/microbiol.2022010.

(6) Omaye, S. T.; David Turnbull, J.; Sauberlich, H. E. Selected Methods for the Determination of Ascorbic Acid in Animal Cells, Tissues, and Fluids. *Methods Enzymol* **1979**, *62* (C), 3–11. https://doi.org/10.1016/0076-6879(79)62181-X.

(7) Sheikhzadeh, E.; Eissa, S.; Ismail, A.; Zourob, M. Diagnostic Techniques for COVID-19 and New Developments. *Talanta* **2020**, *220* (May), 121392. https://doi.org/10.1016/j.talanta.2020.121392.

(8) Hosseini, A.; Pandey, R.; Osman, E.; Victorious, A.; Li, F.; Didar, T.; Soleymani, L. Roadmap to the Bioanalytical Testing of COVID-19: From Sample Collection to Disease Surveillance. *ACS Sens* **2020**, *5* (11), 3328–3345. https://doi.org/10.1021/acssensors.0c01377.

(9) Rajabali, M.; Asgharyan, H.; Naeini, V. F.; Boudaghi, A.; Zabihi, B.; Foroutan, M.; Mohajerzadeh, S. Experimental and Molecular Dynamics Studies of an Ultra-Fast Sequential Hydrogen Plasma Process for Fabricating Phosphorene-Based Sensors. *Sci Rep* **2021**, *11* (1), 1–13. https://doi.org/10.1038/s41598-021-95463-z.

(10) Asgharian, H.; Khodayari, M.; Rajabali, M.; Mohajerzadeh, S. Molecule-Induced n-Type Behavior of Phosphorene-Based Field-Effect Transistor for Highly Sensitive Detection of Sialic Acid. *Electrochim Acta* **2023**, *469* (July), 143228. https://doi.org/10.1016/j.electacta.2023.143228.

(11) Könemund, L.; Neumann, L.; Hirschberg, F.; Biedendieck, R.; Jahn, D.; Johannes, H. H.; Kowalsky, W. Functionalization of an Extended-Gate Field-Effect Transistor (EGFET) for Bacteria Detection. *Sci Rep* **2022**, *12* (1), 1–10. https://doi.org/10.1038/s41598-022-08272-3.

(12) Choi, S.; Park, I.; Hao, Z.; Holman, H. Y. N.; Pisano, A. P. Quantitative Studies of Long-Term Stable, Top-down Fabricated Silicon Nanowire PH Sensors. *Appl Phys A Mater Sci Process* **2012**, *107* (2), 421–428. https://doi.org/10.1007/s00339-011-6754-9.

(13) Fernandes, P. G.; Seitz, O.; Chapman, R. A.; Stiegler, H. J.; Wen, H. C.; Chabal, Y. J.; Vogel, E. M. Effect of Mobile Ions on Ultrathin Silicon-on-Insulator-Based Sensors. *Appl Phys Lett* **2010**, *97* (3), 034103. https://doi.org/10.1063/1.3463453.

(14) Chi, L. L.; Chou, J. C.; Chung, W. Y.; Sun, T. P.; Hsiung, S. K. Study on Extended Gate Field Effect Transistor with Tin Oxide Sensing Membrane. *Mater Chem Phys* **2000**, *63* (1), 19–23. https://doi.org/10.1016/S0254-0584(99)00184-4.

(15) Hung, S.; Cheng, N.; Yang, C.; Lo, Y. Investigation of Extended-Gate Field-Effect Transistor PH Sensors Based on Different-. *Nanoscale Res Lett* **2014**, *9* (502), 1–8.

(16) Jang, H. J.; Gu, J. G.; Cho, W. J. Sensitivity Enhancement of Amorphous InGaZnO Thin Film Transistor Based Extended Gate Field-Effect Transistors with Dual-Gate Operation. *Sens Actuators B Chem* **2013**, *181*, 880–884. https://doi.org/10.1016/j.snb.2013.02.056.

(17) Mishra, A. K.; Jarwal, D. K.; Mukherjee, B.; Kumar, A.; Ratan, S.; Jit, S. CuO Nanowire-Based Extended-Gate Field-Effect-Transistor (FET) for PH Sensing and Enzyme-Free/Receptor-Free Glucose Sensing Applications. *IEEE Sens J* **2020**, *20* (9), 5039–5047. https://doi.org/10.1109/JSEN.2020.2966585.

(18) Chen, C. P.; Ganguly, A.; Lu, C. Y.; Chen, T. Y.; Kuo, C. C.; Chen, R. S.; Tu, W. H.; Fischer, W. B.; Chen, K. H.; Chen, L. C. Ultrasensitive in Situ Label-Free DNA Detection Using a GaN Nanowire-Based Extended-Gate Field-Effect-Transistor Sensor. *Anal Chem* **2011**, *83* (6), 1938–1943. https://doi.org/10.1021/ac102489y.

(19) Zhang, Y.; Sun, C.; Duan, Y.; Cheng, S.; Hu, W. Carbon Dots-Functionalized Extended Gate Organic Field Effect Transistor-Based Biosensors for Low Abundance Proteins. *Nanoscale* **2023**, *15* (40), 16458–16465. https://doi.org/10.1039/d3nr03405d.

(20) Kammarchedu, V.; Asgharian, H.; Zhou, K.; Soltan Khamsi, P.; Ebrahimi, A. Recent Advances in Graphene-Based Electroanalytical Devices for Healthcare Applications. *Nanoscale* **2024,** 16, 12857-12882. https://doi.org/10.1039/d3nr06137j.

(21) Geim, A. K.; Novoselov, K. S. The Rise of Graphene PROGRESS. *Nat Mater* **2007**, *6* (3), 183–191.

(22) Tiwari, S. K.; Mishra, R. K.; Ha, S. K.; Huczko, A. Evolution of Graphene Oxide and Graphene: From Imagination to Industrialization. *ChemNanoMat* **2018**, *4* (7), 598–620. https://doi.org/10.1002/cnma.201800089.

(23) Cao, M.; Fu, A.; Wang, Z.; Liu, J.; Kong, N.; Zong, X.; Liu, H.; Gooding, J. J. Electrochemical and Theoretical Study of π–π Stacking Interactions between Graphitic Surfaces and Pyrene Derivatives. *The Journal of Physical Chemistry C* **2014**, *118* (5), 2650–2659.

(24) Crevillen, A. G.; Pumera, M.; Gonzalez, M. C.; Escarpa, A. The Preferential Electrocatalytic Behaviour of Graphite and Multiwalled Carbon Nanotubes on Enediol Groups and Their Analytical Implications in Real Domains. *Analyst* **2009**, *134* (4), 657–662. https://doi.org/10.1039/b822334c.

(25) K. S. Novoselov et al. Electric Field Effect in Atomically Thin Carbon Films. **2016**, *306* (5696), 666–669.

(26) Li, Z.; Young, R. J.; Backes, C.; Zhao, W.; Zhang, X.; Zhukov, A. A.; Tillotson, E.; Conlan, A. P.; Ding, F.; Haigh, S. J.; Novoselov, K. S.; Coleman, J. N. Mechanisms of Liquid-Phase Exfoliation for the Production of Graphene. *ACS Nano* **2020**, *14* (9), 10976–10985. https://doi.org/10.1021/acsnano.0c03916.

(27) Bahri, M.; Gebre, S. H.; Elaguech, M. A.; Dajan, F. T.; Sendeku, M. G.; Tlili, C.; Wang, D. Recent Advances in Chemical Vapour Deposition Techniques for Graphene-Based Nanoarchitectures: From Synthesis to Contemporary Applications. *Coord Chem Rev* **2023**, *475*, 214910. https://doi.org/10.1016/j.ccr.2022.214910.

(28) Tetlow, H.; Posthuma de Boer, J.; Ford, I. J.; Vvedensky, D. D.; Coraux, J.; Kantorovich, L. Growth of Epitaxial Graphene: Theory and Experiment. *Phys Rep* **2014**, *542* (3), 195–295. https://doi.org/10.1016/j.physrep.2014.03.003.

(29) Beidaghi, M.; Gogotsi, Y. Capacitive Energy Storage in Micro-Scale Devices: Recent Advances in Design and Fabrication of Micro-Supercapacitors. *Energy Environ Sci* **2014**, *7* (3), 867–884. https://doi.org/10.1039/c3ee43526a.

(30) Lin, J.; Peng, Z.; Liu, Y.; Ruiz-Zepeda, F.; Ye, R.; Samuel, E. L. G.; Yacaman, M. J.; Yakobson, B. I.; Tour, J. M. Laser-Induced Porous Graphene Films from Commercial Polymers. *Nat Commun* **2014**, *5*, 5–12. https://doi.org/10.1038/ncomms6714.

(31) Butler, D.; Kammarchedu, V.; Zhou, K.; Peeke, L.; Lyle, L.; Snyder, D. W.; Ebrahimi, A. Cellulose-Based Laser-Induced Graphene Devices for Electrochemical Monitoring of Bacterial Phenazine Production and Viability. *Sens Actuators B Chem* **2023**, *378* (November 2022), 133090. https://doi.org/10.1016/j.snb.2022.133090.

(32) Kammarchedu, V.; Butler, D.; Ebrahimi, A. A Machine Learning-Based Multimodal Electrochemical Analytical Device Based on EMoSx-LIG for Multiplexed Detection of Tyrosine and Uric Acid in Sweat and Saliva. *Anal Chim Acta* **2022**, *1232* (May), 340447. https://doi.org/10.1016/j.aca.2022.340447.

(33) Zhou, K.; Kammarchedu, V.; Butler, D.; Soltan Khamsi, P.; Ebrahimi, A. Electrochemical Sensors Based on MoSx-Functionalized Laser-Induced Graphene for Real-Time Monitoring of Phenazines Produced by Pseudomonas Aeruginosa. *Adv Healthc Mater* **2022**, *11* (19), 2200773. https://doi.org/https://doi.org/10.1002/adhm.202200773.

(34) Chen, X.; Liang, Y.; Tang, N.; Li, C.; Zhang, Y.; Xu, F.; Shi, G.; Zhang, M. Ultrasensitive Sensing Urinary Cystatin C via an Interface-Engineered Graphene Extended-Gate Field-Effect Transistor for Non-Invasive Diagnosis of Chronic Kidney Disease. *Biosens Bioelectron* **2024**, *249* (December 2023), 116016. https://doi.org/10.1016/j.bios.2024.116016.

(35) Sani, E. S.; Xu, C.; Wang, C.; Song, Y.; Min, J.; Tu, J.; Solomon, S. A.; Li, J.; Banks, J. L.; Armstrong, D. G.; Gao, W. A Stretchable Wireless Wearable Bioelectronic System for Multiplexed Monitoring and Combination Treatment of Infected Chronic Wounds. *Sci Adv* **2023**, *9* (12), 1–16. https://doi.org/10.1126/sciadv.adf7388.

(36) Chen, X.; Liang, Y.; Tang, N.; Li, C.; Zhang, Y.; Xu, F.; Shi, G.; Zhang, M. Ultrasensitive Sensing Urinary Cystatin C via an Interface-Engineered Graphene Extended-Gate Field-Effect Transistor for Non-Invasive Diagnosis of Chronic Kidney Disease. *Biosens Bioelectron* **2024**, *249* (January), 116016. https://doi.org/10.1016/j.bios.2024.116016.

(37) Peng, Q.; Zeng, Q.; Wang, F.; Wu, X.; Zhang, R.; Shi, G.; Zhang, M. Multi-Engineered Graphene Extended-Gate Field-Effect Transistor for Peroxynitrite

Sensing in Alzheimer's Disease. *ACS Nano* **2023**, *17* (21), 21984–21992. https://doi.org/10.1021/acsnano.3c08499.

(38) Howe, J. Y.; Rawn, C. J.; Jones, L. E.; Ow, H. Improved Crystallographic Data for Graphite. *Powder Diffr* **2003**, *18* (2), 150–154. https://doi.org/10.1154/1.1536926.

(39) Maheshwari, P. H. Developing the Processing Stages of Carbon Fiber Composite Paper as Efficient Materials for Energy Conversion, Storage, and Conservation. *Mater Sci Energy Technol* **2019**, *2* (3), 490–502. https://doi.org/10.1016/j.mset.2019.04.004.

(40) Islam, M.; Lantada, A. D.; Gómez, M. R.; Mager, D.; Korvink, J. G. Microarchitectured Carbon Structures as Innovative Tissue-Engineering Scaffolds. *Adv Eng Mater* **2020**, *22* (6), 2000083. https://doi.org/10.1002/adem.202000083.

(41) Ferrari, A. C.; Meyer, J. C.; Scardaci, V.; Casiraghi, C.; Lazzeri, M.; Mauri, F.; Piscanec, S.; Jiang, D.; Novoselov, K. S.; Roth, S.; Geim, A. K. Raman Spectrum of Graphene and Graphene Layers. *Phys. Rev. Lett.* **2006**, *97* (18), 187401. https://doi.org/10.1103/PhysRevLett.97.187401.

(42) Mamleyev, E. R.; Heissler, S.; Nefedov, A.; Weidler, P. G.; Nordin, N.; Kudryashov, V. V.; Länge, K.; MacKinnon, N.; Sharma, S. Laser-Induced Hierarchical Carbon Patterns on Polyimide Substrates for Flexible Urea Sensors. *npj Flexible Electronics* **2019**, *3* (1), 2. https://doi.org/10.1038/s41528-018-0047-8.

(43) Cheng, L.; Yeung, C. S.; Huang, L.; Ye, G.; Yan, J.; Li, W.; Yiu, C.; Chen, F. R.; Shen, H.; Tang, B. Z.; Ren, Y.; Yu, X.; Ye, R. Flash Healing of Laser-Induced Graphene. *Nat Commun* **2024**, *15* (1), 1–11. https://doi.org/10.1038/s41467-024-47341-1.

(44) Mikheev K. G.; Zonov R. G.; Syugaev A. V.; Bulatov D. L.; Mikheev G. M. The Effect of Line-by-Line Laser Scanning on the Properties of Laser-Induced Graphene. *Physics of the Solid State* **2022**, *64* (5), 579. https://doi.org/10.21883/pss.2022.05.53520.277.

(45) Lozano-Castelló, D.; Cazorla-Amorós, D.; Linares-Solano, A.; Shiraishi, S.; Kurihara, H.; Oya, A. Influence of Pore Structure and Surface Chemistry on Electric Double Layer Capacitance in Non-Aqueous Electrolyte. *Carbon N Y* **2003**, *41* (9), 1765–1775. https://doi.org/10.1016/S0008-6223(03)00141-6.

(46) Hu, H. Y.; Xie, N.; Wang, C.; Wu, F.; Pan, M.; Li, H. F.; Wu, P.; Wang, X. Di; Zeng, Z.; Deng, S.; Wu, M. H.; Vinodgopal, K.; Dai, G. P. Enhancing the Performance of Motive Power Lead-Acid Batteries by High Surface Area Carbon Black Additives. *Applied Sciences (Switzerland)* **2019**, *9* (1), 186. https://doi.org/10.3390/app9010186.

(47) Huang, X.; Shi, W.; Li, J.; Bao, N.; Yu, C.; Gu, H. Determination of Salivary Uric Acid by Using Poly(3,4-Ethylenedioxythipohene) and Graphene Oxide in a

Disposable Paper-Based Analytical Device. *Anal Chim Acta* **2020**, *1103*, 75–83. https://doi.org/10.1016/j.aca.2019.12.057.

(48) Kammarchedu, V.; Butler, D.; Ebrahimi, A. A Machine Learning-Based Multimodal Electrochemical Analytical Device Based on EMoSx-LIG for Multiplexed Detection of Tyrosine and Uric Acid in Sweat and Saliva. *Anal Chim Acta* **2022**, *1232* (May), 340447. https://doi.org/10.1016/j.aca.2022.340447.

(49) Li, H.; Singh, A.; Bayram, F.; Childress, A. S.; Rao, A. M.; Koley, G. Impact of Oxygen Plasma Treatment on Carrier Transport and Molecular Adsorption in Graphene. *Nanoscale* **2019**, *11* (23), 11145–11151. https://doi.org/10.1039/c9nr02251a.

(50) Kaur, S.; Mager, D.; Korvink, J. G.; Islam, M. Unraveling the Dependency on Multiple Passes in Laser-Induced Graphene Electrodes for Supercapacitor and H2O2 Sensing. *Mater Sci Energy Technol* **2021**, *4*, 407–412. https://doi.org/10.1016/j.mset.2021.09.004.

(51) Ma, H.; Ó'Fágáin, C.; O'Kennedy, R. Antibody Stability: A Key to Performance - Analysis, Influences and Improvement. *Biochimie* **2020**, *177*, 213–225. https://doi.org/10.1016/j.biochi.2020.08.019.

(52) Albarghouthi, F. M.; Semeniak, D.; Khanani, I.; Doherty, J. L.; Smith, B. N.; Salfity, M.; MacFarlane, Q.; Karappur, A.; Noyce, S. G.; Williams, N. X.; Joh, D. Y.; Andrews, J. B.; Chilkoti, A.; Franklin, A. D. Addressing Signal Drift and Screening for Detection of Biomarkers with Carbon Nanotube Transistors. *ACS Nano* **2023,** 18(7), 5698-5711. https://doi.org/10.1021/acsnano.3c11679.

(53) Garland, N. T.; Schmieder, J.; Johnson, Z. T.; Hjort, R. G.; Chen, B.; Andersen, C.; Sanborn, D.; Kjeldgaard, G.; Pola, C. C.; Li, J.; Gomes, C.; Smith, E. A.; Angus, H.; Meyer, J.; Claussen, J. C. Wearable Flexible Perspiration Biosensors Using Laser-Induced Graphene and Polymeric Tape Microfluidics. *ACS Appl Mater Interfaces* **2023**, *15* (32), 38201–38213. https://doi.org/10.1021/acsami.3c04665.

(54) Wu, X.; Gong, K.; Zhao, G.; Lou, W.; Wang, X.; Liu, W. Mechanical Synthesis of Chemically Bonded Phosphorus-Graphene Hybrid as High-Temperature Lubricating Oil Additive. *RSC Adv* **2018**, *8* (9), 4595–4603. https://doi.org/10.1039/c7ra11691h.

(55) Hashemi, S. A.; Mousavi, S. M.; Bahrani, S.; Ramakrishna, S.; Babapoor, A.; Chiang, W. H. Coupled Graphene Oxide with Hybrid Metallic Nanoparticles as Potential Electrochemical Biosensors for Precise Detection of Ascorbic Acid within Blood. *Anal Chim Acta* **2020**, *1107*, 183–192. https://doi.org/10.1016/j.aca.2020.02.018.

(56) Marshall, M.; Zhu, Z.; Harris, R.; Collins, E.; Bowen, K. H. Photoelectron Spectroscopic Study of Ascorbate and Deprotonated Ascorbate Anions Using an Electrospray Ion Source and a Cryogenically Cooled Ion Trap. *Journal of Physical Chemistry A* **2021**, *125* (35), 7699–7704. https://doi.org/10.1021/acs.jpca.1c06540.

(57) Sanglaow, T.; Oungkanitanon, P.; Asanithi, P.; Sutthibutpong, T. Molecular Mechanisms on the Selectivity Enhancement of Ascorbic Acid, Dopamine, and Uric Acid by Serine Oligomers Decoration on Graphene Oxide: A Molecular Dynamics Study. *Molecules* **2021**, *26* (10), 2876. https://doi.org/10.3390/molecules26102876.

(58) Cheng, T.; Shen, D. X.; Meng, M.; Mallick, S.; Cao, L.; Patmore, N. J.; Zhang, H. L.; Zou, S. F.; Chen, H. W.; Qin, Y.; Wu, Y. Y.; Liu, C. Y. Efficient Electron Transfer across Hydrogen Bond Interfaces by Proton-Coupled and -Uncoupled Pathways. *Nat Commun* **2019**, *10* (1), 1–10. https://doi.org/10.1038/s41467-019-09392-7.

(59) Sheibani, S.; Capua, L.; Kamaei, S.; Akbari, S. S. A.; Zhang, J.; Guerin, H.; Ionescu, A. M. Extended Gate Field-Effect-Transistor for Sensing Cortisol Stress Hormone. *Commun Mater* **2021**, *2* (1), 1–10. https://doi.org/10.1038/s43246-020-00114-x.

(60) Seo, G.; Lee, G.; Kim, M. J.; Baek, S. H.; Choi, M.; Ku, K. B.; Lee, C. S.; Jun, S.; Park, D.; Kim, H. G.; Kim, S. J.; Lee, J. O.; Kim, B. T.; Park, E. C.; Kim, S. Il. Rapid Detection of COVID-19 Causative Virus (SARS-CoV-2) in Human Nasopharyngeal Swab Specimens Using Field-Effect Transistor-Based Biosensor. *ACS Nano* **2020**, *14* (4), 5135–5142. https://doi.org/10.1021/acsnano.0c02823.

(61) Kang, H.; Wang, X.; Guo, M.; Dai, C.; Chen, R.; Yang, L.; Wu, Y.; Ying, T.; Zhu, Z.; Wei, D.; Liu, Y.; Wei, D. Ultrasensitive Detection of SARS-CoV-2 Antibody by Graphene Field-Effect Transistors. *Nano Lett* **2021**, *21* (19), 7897–7904. https://doi.org/10.1021/acs.nanolett.1c00837.

(62) Protein, S.-S.; Laser, U.; Graphene, I.; Ren, T. Field-Effect Transistor. **2021**.

(63) Michen, B.; Graule, T. Isoelectric Points of Viruses. *J Appl Microbiol* **2010**, *109* (2), 388–397. https://doi.org/10.1111/j.1365-2672.2010.04663.x.

(64) Barton, H. A. Safe and Effective Disinfection of Showcave Infrastructure in a Time of COVID-19. *Int J Speleol* **2020**, *49* (2), 137–147. https://doi.org/10.5038/1827-806X.49.2.2332.

(65) Bae, M.; Kim, H. The Role of Vitamin C, Vitamin D, and Selenium in Immune System against COVID-19. *Molecules* **2020**, *25* (22), 1–12. https://doi.org/10.3390/MOLECULES25225346.

(66) Wirojsaengthong, S.; Chailapakul, O.; Tangkijvanich, P.; Henry, C. S.; Puthongkham, P. Size-Dependent Electrochemistry of Laser-Induced Graphene Electrodes. *Electrochim Acta* **2024**, *494* (May), 144452. https://doi.org/10.1016/j.electacta.2024.144452.

(67) Bard, A. J.; Faulkner, L. R. Fundamentals and Applications. *Electrochemical methods* **2001**, *2* (482), 580–632.

(68) Khamsi, P. S.; Kammarchedu, V.; Ebrahimi, A. Evaporation-Enhanced Redox Cycling for Rapid Detection of Attomolar SARS-CoV-2 Virions Using

Nanolithography-Free Electrochemical Devices. *OSF* **2024**. https://doi.org/https://doi.org/10.1149/osf.io/j5qxk.

(69) Kim, J.; Imani, S.; de Araujo, W. R.; Warchall, J.; Valdés-Ramírez, G.; Paixão, T. R. L. C.; Mercier, P. P.; Wang, J. Wearable Salivary Uric Acid Mouthguard Biosensor with Integrated Wireless Electronics. *Biosens Bioelectron* **2015**, *74*, 1061–1068. https://doi.org/10.1016/j.bios.2015.07.039.

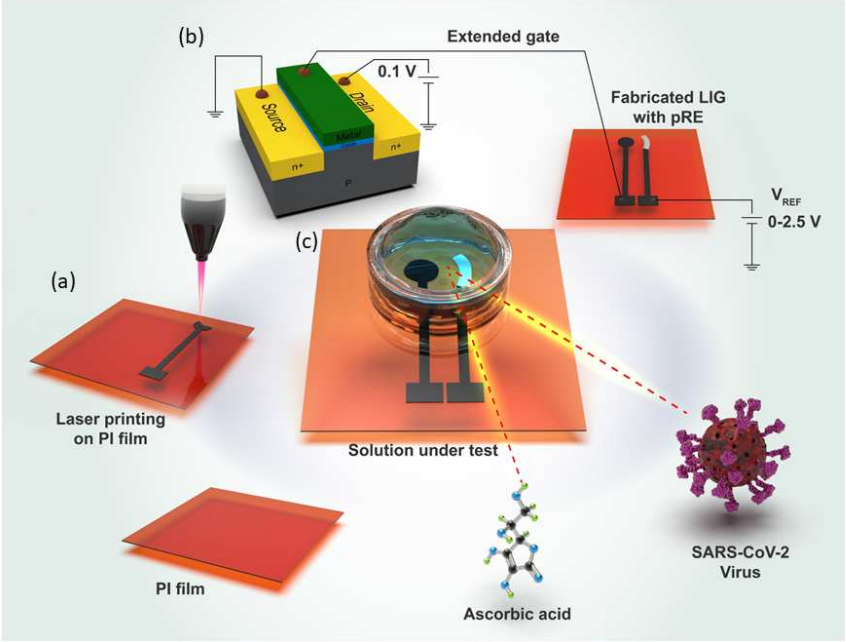

Figure 1. Schematic of the EGFET device fabrication steps. **(a)** The sensing part (gate) of the EGFET is fabricated by converting the polyimide (PI) sheet to laser induced graphene (LIG) using CO_2 laser. **(b)** Configuration of the EGFET device with the LIG-based gate and a commercial NMOS as the transducer. **(c)** Completed EG with the solution under test consisting of AA or SARS-CoV-2 antigens or virion mimics. ρRE = pseudo-reference electrode made of silver paste-LIG.

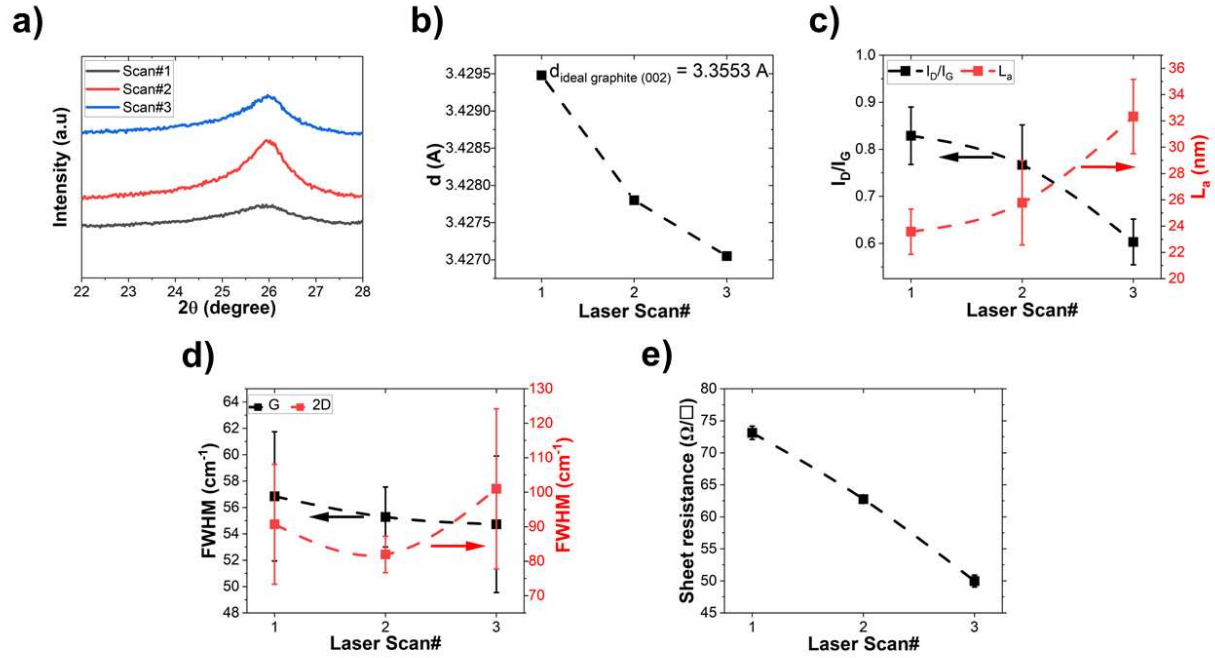

Figure 2. Material characterization of fabricated LIG using different laser scan number. **(a)** X-ray diffraction (XRD) analysis of LIG powder scraped from polyimide film. **(b)** Interlayer spacing between (002) graphitic crystal planes extracted via XRD. **(c)** Intensity ratio ($\frac{I_D}{I_G}$) and crystallite size (L_a) obtained from Raman spectra. The error bars show the standard errors with n=3. **(d)** FWHM of G and 2D peaks extracted from the Raman spectra. The error bars show the standard errors with n=3. **(e)** Sheet resistance of LIG as a function of laser scan number. The error bars show the standard errors with n=4.

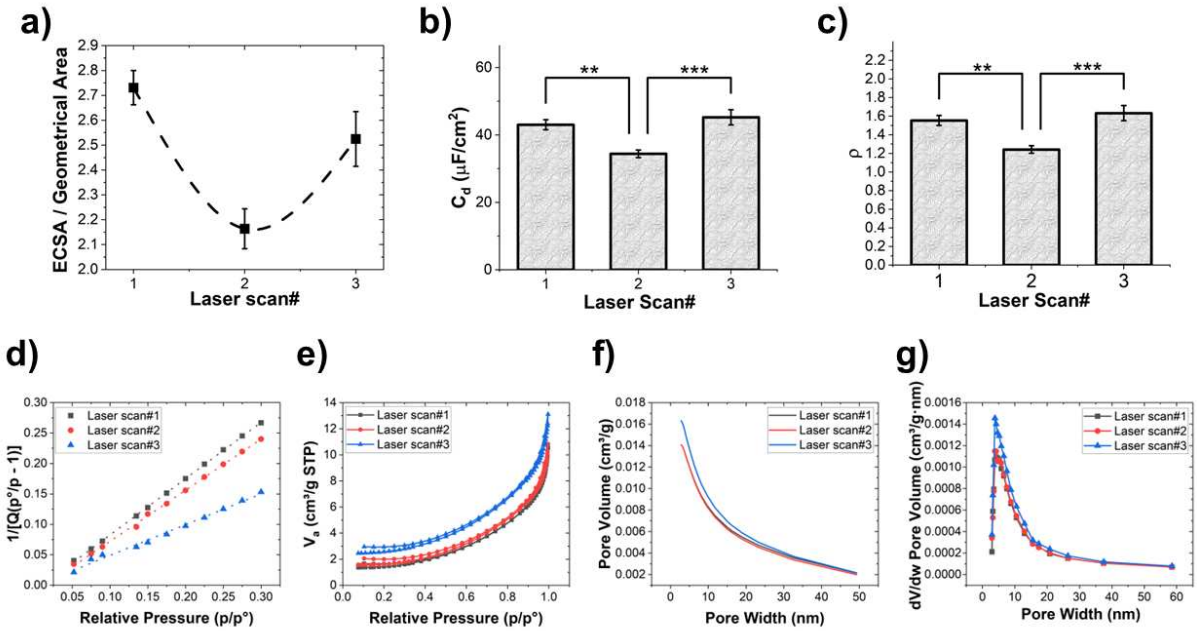

Figure 3. Porosity and surface area characteristics of LIG with different laser scan number. **(a)** Normalized electrochemical active surface area (ECSA) to geometrical area. **(b)** Double-layer capacitance (C_d) is calculated from the background charging current. **(c)** calculated roughness factor from the double-layer capacitance. The error bars show the standard errors with n=4. **(d)** Brunauer-Emmett-Teller (BET) surface area plot. **(e)** BET plot of the N_2 adsorption–desorption isotherm. **(f)** Barrett-Joyner-Halenda (BJH) desorption cumulative pore volume **(g)** BJH desorption $\frac{dV}{dw}$ pore volume.

Table 1. Surface area and pore structure parameters of LIG with different laser scan#.

Laser Scan#	BET Surface Area ($\frac{m^2}{g}$)	BJH cumulative surface area ($\frac{m^2}{g}$)	BJH cumulative volume of pores ($\frac{Cm^3}{g}$)	BET average pore diameter (nm)	BJH average pore diameter (nm)
1	4.7512	5.7623	0.014095	12.9708	9.7842
2	5.2644	5.8240	0.014071	12.0105	9.6638
3	8.3063	7.0377	0.016339	9.2225	9.2868

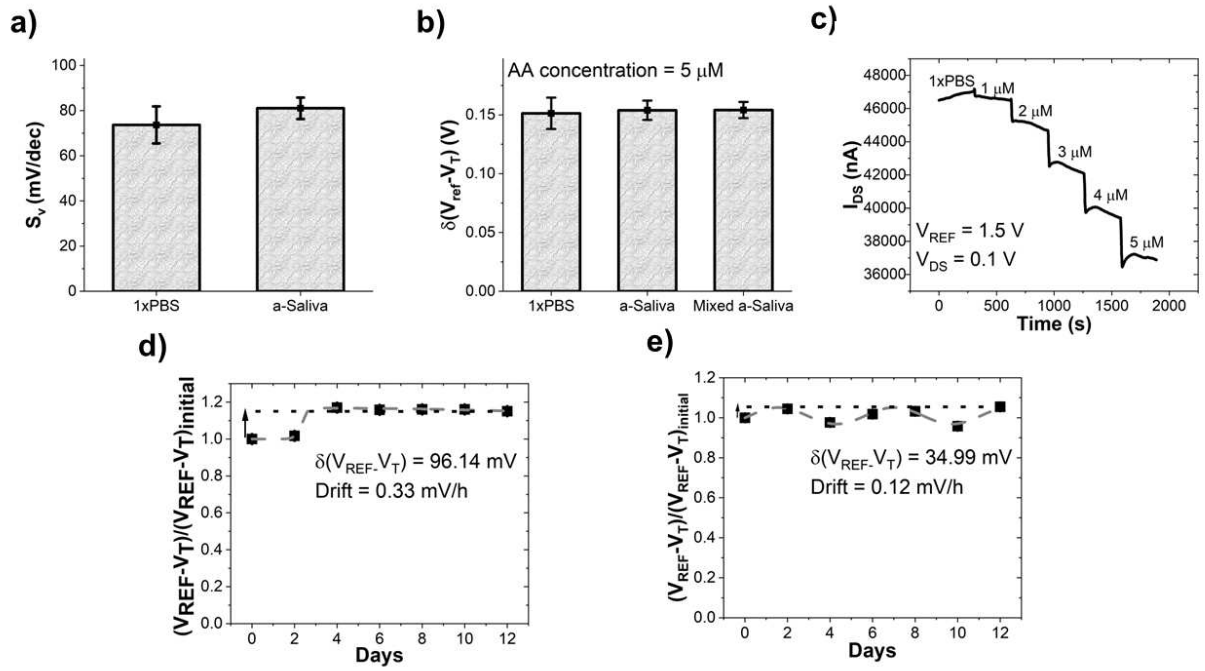

Figure 4. Characterizing EGFET response to ascorbic acid (AA) using 2-pass LIG as the extended gate. **(a)** Comparison of sensitivity (S_v) to AA (10 nM-10 μM) in 1×PBS and a-saliva. **(b)** Baseline-subtracted value of the gate voltage ($\delta(V_{REF}-V_T)$) at $I_{DS} = 95\mu A$ in 1×PBS, a-saliva, and mixed a-saliva to show selectivity toward AA. Mixed a-saliva consists of 300 pM dopamine, 200 μM uric acid, and 300 μM tyrosine. **(c)** Real time measurement ($V_{REF} = 1.5\,V$, and $V_{DS} = 0.1\,V$) of the EGFET device in response to different AA concentrations with the step of 1 μM in 1×PBS added every 5 minutes. **(d)** Reusability (dashed line represents Bigaussian fit) and **(e)** shelf life (dashed line represents SineDamp fit) tests within 12 days in constant AA concentration (5 μM). The error bars show the standard errors with n = 9.

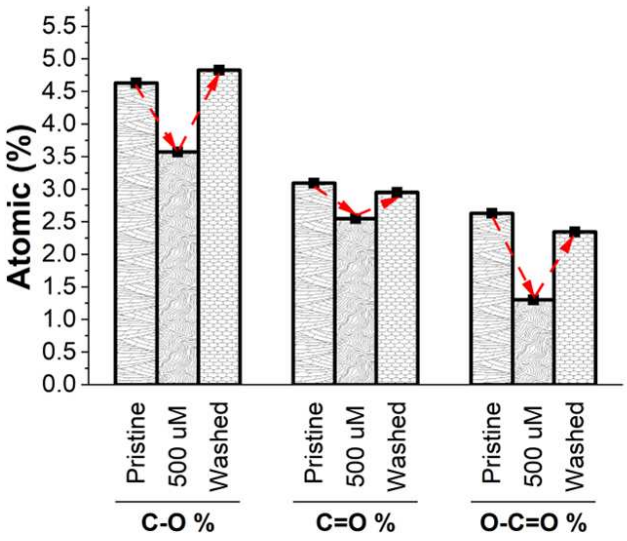

Figure 5. Comparison of the atomic concentrations of carbon species (in atom% of carbon) of pristine LIG, different concentrations of AA (500 µM, 50 µM, and 5 µM) in 1×PBS before and after washing LIG. C–O: hydroxyl functional group, C═O: carbonyl functional group, and O–C═O: carboxyl functional group. Arrow shows the oxygen functional groups decrease after adding AA to the LIG and recover to its initial value after washing with 1×PBS.

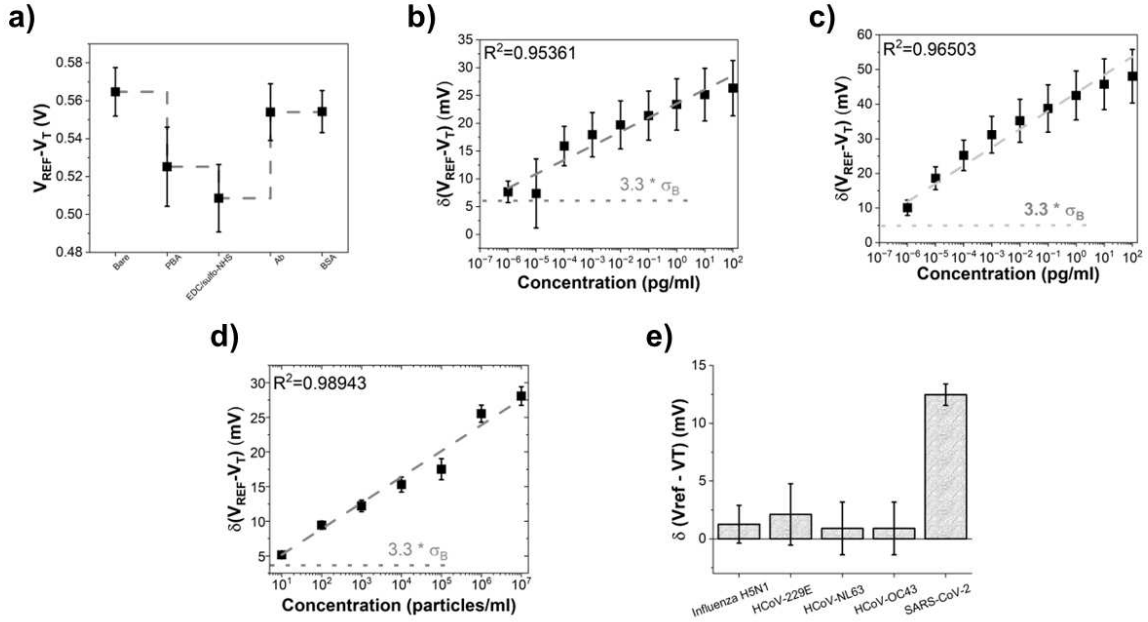

Figure 6. Virus detection using EGFET sensors. **(a)** Characterization of the EGFET sensor after each functionalization step for detecting SARS CoV-2 S protein antigen. **(b)** Baseline-subtracted value of the gate voltage at $I_{DS} = 95\mu A$ in 1×PBS to compare the sensitivity of LIG with 1 laser scanning (1-pass LIG) and **(c)** 2 laser scanning (2-pass LIG). **(d)** Response to SARS-CoV-2 S mimics calculated based on the baseline-subtracted gate voltage at $I_{DS} = 95\mu A$ in 1×PBS with 2-pass LIG. **(e)** Baseline-subtracted value of the gate voltage at $I_{DS} = 95\mu A$ in 1×PBS to show selectivity of device toward SARS CoV-2 S mimics against other viruses including influenza H5N1, human coronaviruses HCoV-229E, HCoV-NL63, HCoV-OC43, using 2-pass LIG at constant concentration of $10^4 \frac{particles}{ml}$. In parts (b)-(d), the dashed line represents linear fitting, and the dotted line (σ_B) represents the standard deviation of the blank solutions. The error bars show the standard errors with n = 9 for SARS CoV-2 S protein antigen and n=18 for SARS CoV-2 S mimics. In part (e), the error bars show the standard errors with n = 21 for non-targets and n = 18 for target (SARS CoV-2 S mimics).

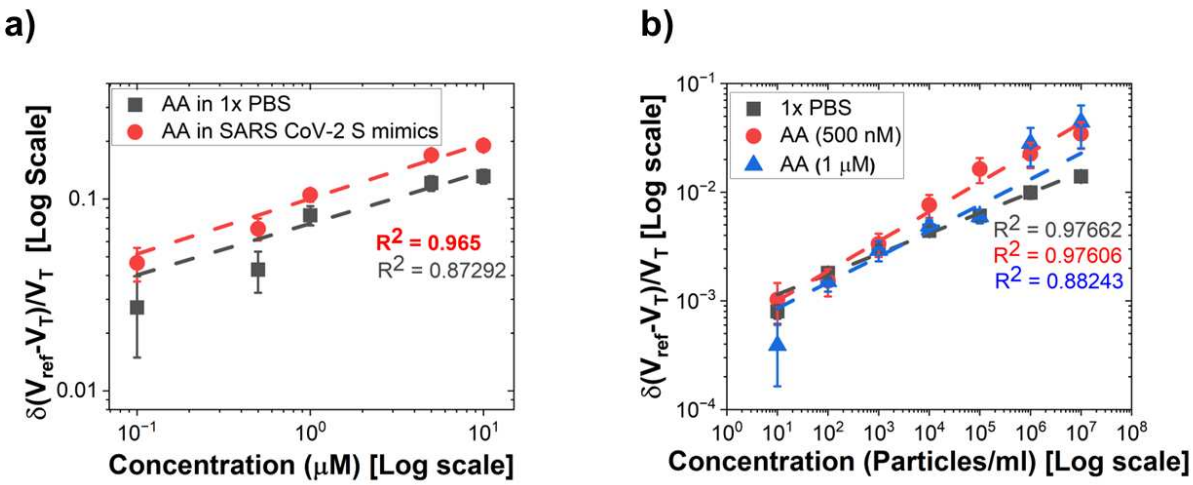

Figure 7. Detection of AA and SARS CoV-2 virion mimics in the presence of the other molecule. Normalized baseline-subtracted value of the gate voltage at $I_{DS} = 95$ μA to show the device sensitivity to **(a)** AA or its mixture with 10^5 $\frac{particles}{ml}$ SARS-CoV-2 mimics in 1× PBS and **(b)** SARS-CoV-2 mimics or its mixture with 500 nM and 1 μM AA in 1× PBS. The error bars show the standard errors with n = 9 for part (a) and n=12 for part (b). The data are plotted on a logarithmic scale to better highlight the performance at low analyte concentrations. The dashed line represents linear fitting.

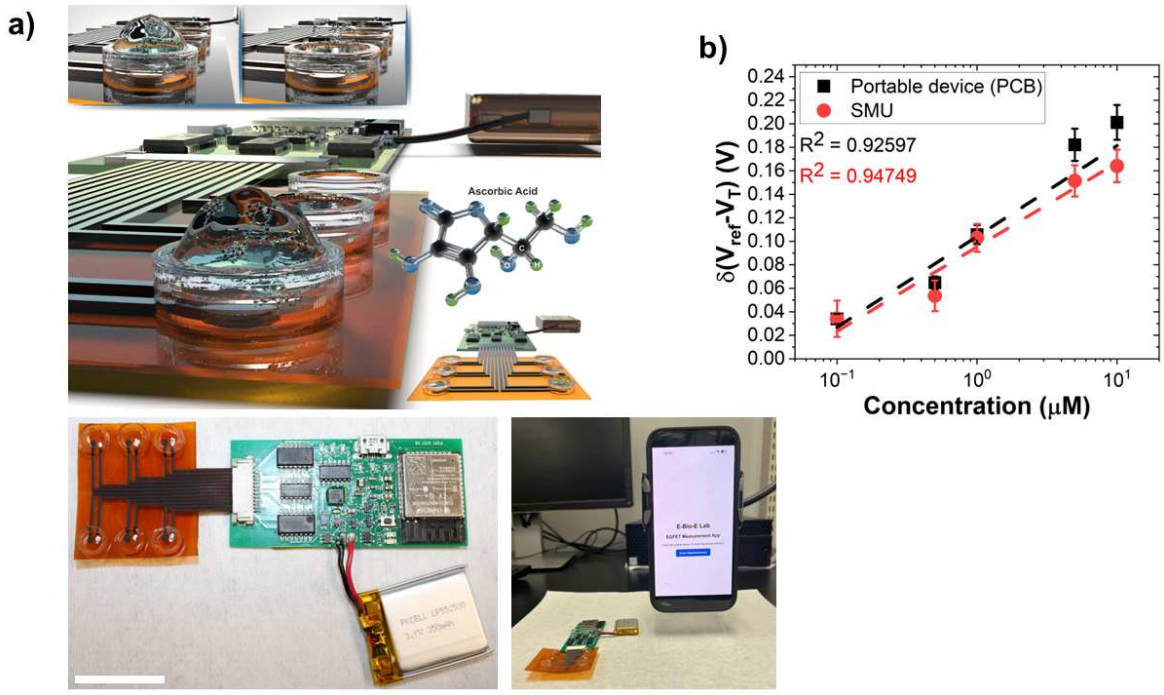

Figure 8. Proposed portable and wireless multi-extended gate electrodes. **(a)** Schematic and optical images of the developed portable and wireless multi-EG electrode chip. The scale bar is 2.5 cm. **(b)** Comparison of the calibration curves (baseline-subtracted value of the gate voltage at $I_{DS} = 95$ μA in 1×PBS) collected using the source meter unit (SMU) and portable PCB board for detecting AA.

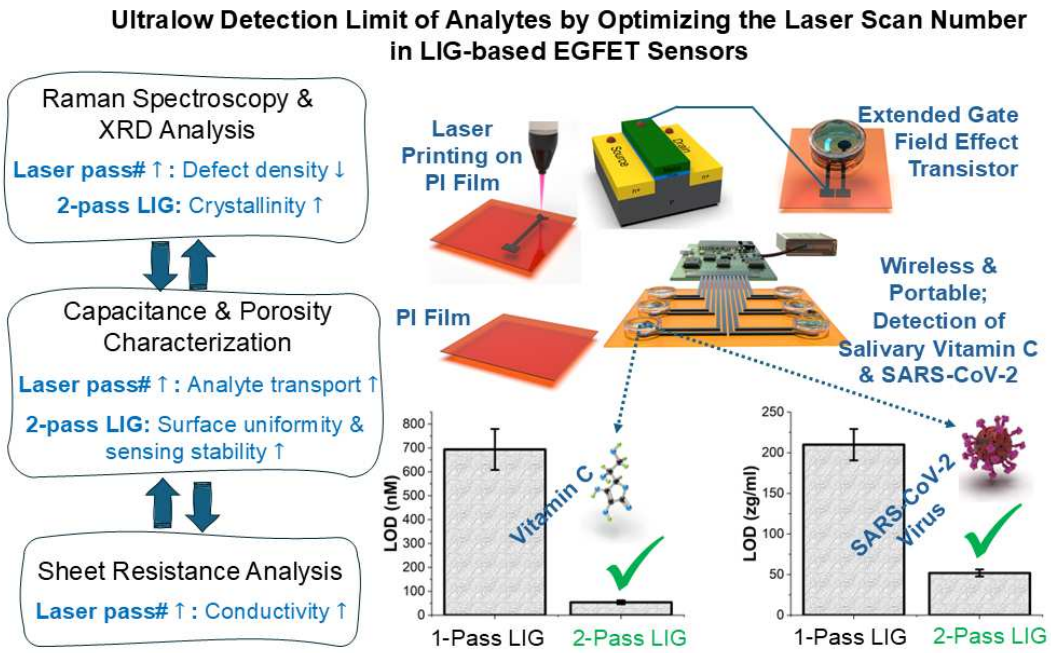

For Table of Contents Only